Nonlinear mechanical behaviour of $Ba_{0.5}Sr_{0.5}Co_{0.8}Fe_{0.2}O_{3-\delta}$ and *in situ* stress dependent synchrotron X-ray diffraction study

Philipp T. Geiger[1], Oliver Clemens[2,3], Neamul H. Khansur[1], Manuel Hinterstein[4], Mtabazi G. Sahini[5], Tor Grande[5], Patrick Tung[6], John E. Daniels[6], Kyle G. Webber[1]

[1]Department of Materials Science, Friedrich-Alexander Universität Erlangen-Nürnberg, Martensstr. 5, 91058 Erlangen, Germany

[2]Technische Universität Darmstadt, Joint Research Laboratory Nanomaterials, Jovanka Bontschits Str. 2, 64287 Darmstadt, Germany

[3] Karlsruher Insitut für Technologie, Institut für Nanotechnologie, Hermann-von-Helmholtz-Platz 1, 76344 Eggenstein-Leopoldshafen, Germany

[4] Karlsruher Insitut für Technologie, Institut für Angewandte Materialien (IAM-KWT), Haid-und-Neu Str. 7, 76131 Karlsruhe, Germany

[5]Department of Materials Science and Engineering, Norwegian University of Science and Technology, NO-7491 Trondheim, Norway

[6]School of Materials Science and Engineering, UNSW Australia, Sydney, New South Wales 2052, Australia

Abstract

Perovskite type $Ba_{0.5}Sr_{0.5}Co_{0.8}Fe_{0.2}O_{3-\delta}$ ceramics display nonlinear stress-strain behaviour upon uniaxial compression at room temperature. Step functional loading experiments show that the nonlinear strain response of the material is time dependent, partially reversible and depends on the oxygen vacancy concentration. *In situ* compressive stress-dependent synchrotron X-ray diffraction reveals that the nonlinearity is not related to ferroelasticity or a stress-induced phase transformation. The oxygen vacancy concentration and average spin state were determined from Rietveld analysis of the magnetic scattering found in the neutron powder diffraction data, indicating their role during mechanical loading. An oxygen vacancy migration

model and a spin-state transition are proposed as possible mechanisms of nonlinear mechanical response.

1. Introduction

$Ba_{0.5}Sr_{0.5}Co_{0.8}Fe_{0.2}O_{3-\delta}$ (BSCF) ceramics have received a great deal of attention due to the high mixed ionic and electronic conductivity and oxygen permeation rate at intermediate temperatures [1,2]. These properties make BSCF an interesting material for solid oxide fuel cell cathodes and gas permeation membranes [3,4]. Importantly, the coefficient of thermal expansion increases with ionic conductivity [5] and was found to be about 20×10^{-6} K^{-1} for BSCF [6,7]. This is significantly higher than found for materials in solid oxide fuel cell components [2], which can result in thermal expansion mismatch and subsequent large internal mechanical stresses that may lead to material degradation, creep, and eventual failure [8]. In addition, mechanical stresses can also influence the ionic conductivity of solid oxygen electrolytes [9–11].

The remarkably high ionic conductivity in BSCF ($\sigma_o = 1.8 – 7 \times 10^{-2}$ S cm^{-1} at 700°C [1,12,13]) originates from the significant oxygen non-stoichiometry (δ), which facilitates ionic transport. Conventional oxygen ion conductors such as yttria stabilised zirconia have defect concentrations up to 10% ($\delta = 0.1$). In contrast, various techniques revealed that BSCF exhibits a δ between 0.2 and 0.8, depending on temperature, oxygen partial pressure and composition [2,4,6–8,12,14,15]. Generally, it is accepted that δ can exceed 0.5, which corresponds to one out of six oxide ions, coordinating a B-site cation, being unoccupied in average. At elevated temperatures, such as 550 ºC and above, BSCF exchanges oxygen with the surrounding atmosphere through the surface, resulting in an increase of the oxygen vacancy concentration, enhancing the entropy. This is accompanied by a small distortion of the unit cell and measurable macroscopic strain. This phenomenon,

known as chemical strain, is based on uncompensated cationic coulomb repulsion due to the absence of an oxide ion. In addition, the radius of the multivalent B-site cation increases on reduction [14].

Many perovskite crystals display a nonlinear mechanical constitutive behaviour. Ferroelastic ceramics, such as ZrO_2 [16], $Pb(Zr_xTi_{1-x})O_3$ [17], and $La_{0.58}Sr_{0.4}Co_{0.2}Fe_{0.8}O_{3-\delta}$, [19] show a remanent strain during mechanical loading due to the switching of ferroelastic domains. In these materials, the central B-site cation is mechanically reoriented ("switched") to another energetically more favourable crystallographic orientation. The switching process in real materials is the result of a domain nucleation and growth processes, where the domain walls separate regions of like polarization. The domain walls are sensitive to mechanical stress and can be swept through the crystal. Upon the release of the compressive stress, some domains will remain in the ferroelastically switched configuration, leaving the material with a macroscopic remanent strain [18]. Importantly, ferroelasticity is found below the Curie point, which separates the high temperature paraelectric phase from the lower temperature ferroelectric phase. Other perovskite crystals have been observed to undergo a stress-induced phase transformation to a different crystallographic symmetry during mechanical loading. This effect has been observed in single crystal ferroelectric perovskites, such as $Pb(Mg_{1/3}Nb_{2/3})O_3$-$PbTiO_3$ [19,20] and $BaTiO_3$ [21], as well as polycrystalline materials near structural phase transition boundaries [22,23]. Ferroelasticity and stress-induced phase transformation have both been previously investigated by stress dependent X-ray and neutron diffraction techniques, giving insight into the effect of stress on the crystallographic structure [23–26].

The cubic phase of BSCF is metastable between room temperature and ~700°C [27] and, unlike the related $SrCo_{0.8}Fe_{0.2}O_{3-\delta}$ below 790 °C, does not show

symmetry lowering from oxygen vacancy ordering [28]. BSCF slowly but reversibly forms a hexagonal polymorph at the grain boundaries below 850 °C [29], which has strong influence on the mechanical behaviour and ionic conductivity at these temperatures [12,27,30–32]. Above 900 °C the cubic phase is stable [32,33]. The formation of the hexagonal phase at the desired temperatures and the low ionic conductivity of that phase are considered to be one of the biggest obstacles for the implementation of BSCF in fuel cell applications [34,35].

Previous experimental investigations on the mechanical behaviour of BSCF revealed a time- and temperature-dependent remanent strain during compressive loading at relatively low stress levels [36]. This observation was attributed to a stress-induced spin state transition, which corresponds well to an elastic anomaly of BSCF found between room temperature and ~300 °C by Huang *et al.* [37]. In this temperature range, the elastic modulus decreases with increasing temperature, going through a minimum at 200 °C and recovering at approximately 300 °C. Corresponding temperature-dependent susceptibility measurements suggest a spin state transition of the central Co^{3+} ion in this temperature range [38,39]. In addition, Araki *et al.* [36] investigated the stress-strain behaviour of BSCF at relatively small loads (≤ 106 MPa) and found room temperature creep and a remanent strain. These phenomena were attributed to a spin-state transition as well [40]. It was suggested that the compressive stress results in a tetragonal distortion of the unit cell, reducing the crystal field splitting energy and, therefore, making a high spin state energetically more favourable. However, the possible influence of oxygen vacancies was not considered in this work.

In this study, the room temperature mechanical constitutive behaviour of BSCF is investigated under compressive loading. The loading rate was varied in

order to show the time-dependent nature of the nonlinear mechanical behaviour. In addition, BSCF samples were thermally treated in air and nitrogen atmospheres to determine the effect of the oxygen non-stoichiometry, which has not been addressed yet in regards of the elastic properties. The experimental macroscopic constitutive behaviour is contrasted to *in situ* stress-dependent synchrotron diffraction experiments to determine the crystal structure during mechanical loading. Additional powder neutron diffraction measurements were performed to characterize the oxygen vacancy concentration of BSCF annealed under various atmospheres as well as the average spin state from the magnetic scattering contribution.

2. Experimental Methodology

Two different BSCF powders were used in this work. The first BSCF powder was prepared by spray pyrolysis of aqueous solutions of the respective nitrates with stoichiometric amounts of cations as described by Švarcová *et al.* [41]. The as-synthesized powder was calcined at 900 C for 24 hr followed by ball-milling in isopropanol for 24 h. This powder will be referred to as BSCF-BC in the following discussion, as an impurity phase was found. The second powder was a commercial BSCF powder (Treibacher AG, Austria) and will be referred to as BSCF. Cylindrical samples were produced from both powders by cold isostatic pressing at 350 MPa, followed by sintering. The sintering was performed for 12 hr at 1050°C with a constant cooling rate of 1.75°C/min to room temperature. Following sintering, cylinders with a height of 6 mm and diameter of 5.8 mm were ground from the dense bodies. Care was taken to ensure the circular faces were even and parallel, which was achieved with a surface grinder. For *in situ* synchrotron experiments cylinders with height of 2 mm and diameter of 1 mm were produced using the same procedure.

Following grinding, each sample was annealed for 2 hr at 900°C in order to relax residual stresses and reset possibly machining induced changes to the material.

Crystallographic information was obtained from both laboratory X-ray and neutron diffraction. Laboratory XRD was performed with a Siemens Kristalloflex D500 diffractometer, using $Cu_{K\alpha}$ radiation. Prior to the measurement, the BSCF-BC powder was annealed in air, whereas the BSCF powder was annealed at 1 atm in air and nitrogen (99.99% purity). The nitrogen contained ≤ 3 ppm oxygen, resulting in an oxygen partial pressure of less than $3 \cdot 10^{-3}$ mbar. Neutron diffraction data was recorded on the BSCF powder at the Wombat beamline [42], a neutron diffractometer at the Australian Nuclear Science and Technology Organisation (ANSTO) in Sydney, Australia. Data was collected with a curved position sensitive detector, using monochromatic radiation with a wavelength of λ = 1.63 Å. Analysis of neutron diffraction data was performed with the program TOPAS 5.0 [43]. A modified pseudo Voigt function was used to model the angular dependence of the peak shape. The nuclear reflections were refined using a structural model of the cubic perovskite type structure (space group $Pm\bar{3}m$) with site occupancies of the cation sites being fixed according to the sample composition. The occupancy of the anion site was refined independently, with the thermal parameters of all the atoms on all the crystallographic sites being constrained to be the same. The magnetic scattering could be described by adding a second phase with G-type antiferromagnetic order (with a very characteristic pattern according to our previous experience [44]), which was constrained to the identical structural and microstructural parameters as the nuclear phase and for which only the absolute of the magnetic vector was refined for the G-type setting to describe the relative intensities of the magnetic reflections.

Mechanical testing was performed on both compositions with a screw-type load frame (Zwick/Roell Z030) outfitted with a linear variable differential transformer used to measure the sample displacement under load. The setup is described in detail elsewhere [45]. During mechanical testing the compressive stress was applied in a triangular waveform with a loading/unloading rate of ±5 MPa/s up to a maximum stress of -500 MPa. A preload of -3.8 MPa was used to ensure sample contact prior to testing. A second test was performed by applying a step functional loading program. The load was rapidly increased with a rate of -500 MPa/s up to -500 MPa and then kept constant up for 5 min. Following the holding time, the stress was reduced back to preload with a rate of 500 MPa/s and held at the preload for 5 min. The holding times were used to observe the time-dependent relaxation. Mechanical testing was performed on samples annealed in air and nitrogen in order to compare different oxygen non-stoichiometry levels.

Stress-dependent synchrotron X-ray diffraction measurements were performed at the ID15 beamline of the European Synchrotron and Radiation Facility in Grenoble, France. A compact load frame with a piezoelectric stack was used to apply load while the sample was in the beam line. The piezoelectric actuator was controlled by a function generator after manually adjusting a small preload of approximately -17 MPa. A triangular loading program was applied with a maximum load of -720 MPa. A lower loading rate of approximately -0.5 MPa/s was chosen in order to increase the temporal resolution. These conditions were later reproduced in a macroscopic measurement with the Zwick/Roell Z030 for comparison. A monochromatic X-ray beam with an energy of ~73 keV (wavelength $\lambda \approx 0.1705$ Å) was used. The transmitted diffraction pattern was measured with a Pixium 4700 flat panel detector [46]. This experimental setup enables collection of fully orientation dependent data

with respect to the angle between the scattering vector and applied field vector in a single diffraction image. Details of the experimental setup have been reported previously [23,26]. The collected intensities were integrated over 10 s and correlated to the average stress on the sample. The data was collected for azimuth angles from 0 to 360° and averaged over 10° segments using the software package Fit2D [47]. Full powder pattern decomposition was performed with the program TOPAS 3.0 (Bruker AXS, Karlsruhe, Germany) [48]. The instrumental intensity distribution for the X-ray data was determined empirically from a fundamental parameters set [49], using a reference scan of CeO_2 (NIST 674b). Each reflection belonging to the cubic perovskite type BSCF phase was fitted to an independent pseudo-Voigt function to adjust for sample dependent reflection broadening and to determine the exact reflection positions. Potential zero errors respectively sample displacement errors (which would influence the positions of the reflections) were determined for the sample without load using the Rietveld method and found to be negligibly small.

3. Results and discussion

3.1 Crystallographic structure

X-ray diffraction patterns for BSCF-BC and BSCF powders are shown in Figure 1. Both the BSCF-BC and BSCF powders show perovskite reflections, which can be indexed with a cubic unit cell. The BSCF-BC powder shows traces of secondary phase. Full pattern Rietveld refinement of the X-ray diffraction data indicates that the BSCF-BC contains 10 wt-% $Ba_3Co_{10}O_{17}$ ($R\bar{3}m$), which is an intergrowth structure of CdI_2 type and perovskite type layers. Lattice parameters of this secondary phases were found to be a = 5.679(1) Å and c = 36.009(7) Å, being in agreement with

previous reports. The compound is known to be paramagnetic at room temperature [50]. In comparison, the commercial BSCF powder was found to contain a single cubic perovskite phase with lattice parameters of a_{air} = 3.9827(1) Å and a_{N2} = 3.9840(1) Å, after annealing the powder in air and nitrogen, respectively. BSCF powder annealed in nitrogen atmosphere shows slight increase in the unit cell volume over that of the powder annealed in air atmosphere.

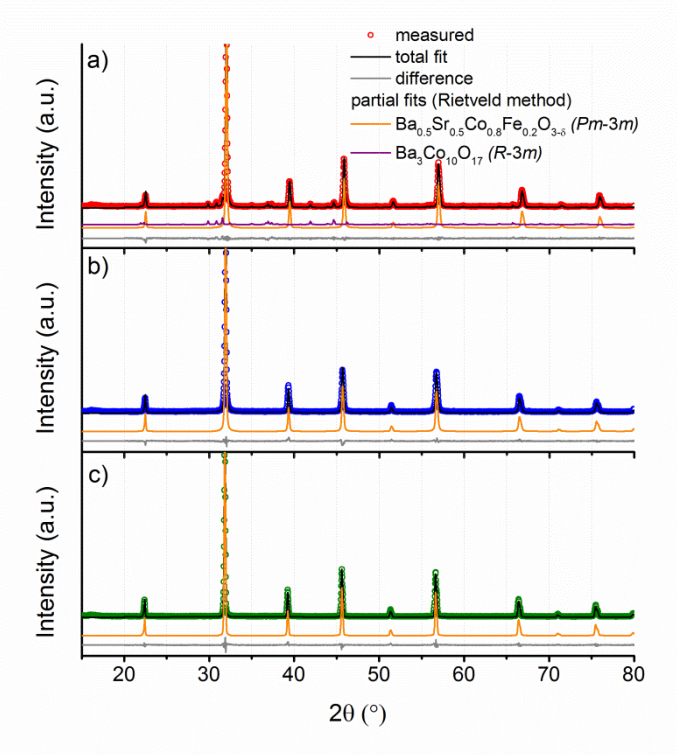

Fig. 1: a) Powder x-ray diffraction patterns of BSCF-BC powder annealed in air, contains an impurity phase, which is found to be $Ba_3Co_{10}O_{17}$ [50]. The commercial BSCF powder annealed in b) air and c) nitrogen purely consists of the cubic perovskite phase.

Neutron diffraction data was collected for the same batch of BSCF powder (annealed in air and nitrogen atmosphere) to investigate the oxygen vacancy concentration. The measured and calculated neutron diffraction patterns are shown in Figure 2. The structural information was obtained from the full pattern Rietveld analysis of the neutron diffraction data. In addition to the lattice parameter,

information regarding oxygen vacancy concentration and magnetic moment was also obtained. The lattice parameter is found to be a_{air} = 3.963(7) Å and a_{N2} = 3.970(6) Å. The oxygen vacancy concentration is determined to be δ_{air} = 0.63(2), which increases to δ_{N2} = 0.70(2) when annealed in nitrogen. The magnetic structure corresponds to a G-type antiferromagnetic order with an average magnetic moment of $|\vec{M}_{air}|$ = 2.33(2) μ_B and $|\vec{M}_{N_2}|$ = 2.61(2) μ_B per B-site cation for powder samples annealed in air and nitrogen, respectively. All of the above structural information indicates that the annealing environment plays a significant role on the structural chemical properties, hence, most likely on the mechanical properties at macroscopic scale.

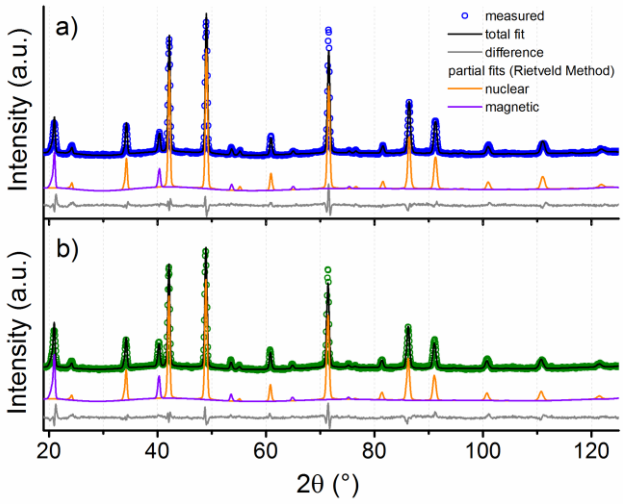

Figure 2: Neutron diffraction patterns of BSCF powder annealed in a) air and b) nitrogen.

3.2 Stress-Strain Behaviour

The mechanical constitutive behaviour of BSCF-BC and BSCF samples annealed in air was characterized at room temperature (Fig. 3). During measurement, a triangular loading program with a maximum stress of –500 MPa and a loading rate of -5 MPa/s was used. Please note that in the following discussion the typical convention is

adopted, where compressive stresses and strains are negative and tensile stresses and strains are positive. At the maximum load of –500 MPa a maximum strain of –0.63% and –0.56 % is found for the BSCF and BSCF-BC, respectively. A unique feature of both BSCF compositions, shown by this measurement, is that the strain after unloading is not zero, but –0.03%. It should be mentioned here that despite containing 10 wt-% secondary phase, BSCF-BC sample displayed the same remanent strains BSCF. This indicates that the 10 wt-% secondary phase in BSCF-BC does not have a significant impact on the remanent state. For comparison, the stress-strain behaviour of polycrystalline Al_2O_3 measured under the same condition is also shown, which displays zero remanent strain. This proves that the remanent strain of the BSCF materials is not based on a measurement error. Phenomenologically, the stress-strain behaviour of both BSCF-BC and BSCF appear similar to ferroelastic perovskite materials like $Pb(Zr,Ti)O_3$ (PZT) or $BaTiO_3$, marked by nonlinearity and a remanent strain. In the present experiments, however, there is no indication of a clear saturation behaviour, characteristic of ferroelasticity [24]. In addition, ferroelastic switching is unlikely, as BSCF exhibits cubic symmetry at room temperature.

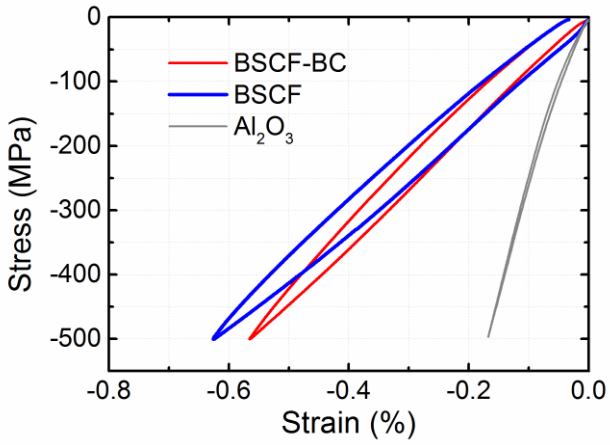

Figure 3. Stress-strain behaviour of air-annealed BSCF-BC and BSCF up to –500 MPa at room temperature. The stress-strain behaviour of polycrystalline Al_2O_3 measured under the same conditions is shown for comparison.

A similar experiment was performed on air-annealed BSCF-BC and BSCF using a step functional loading program, where the loading rate was increased to –500 MPa/s. The stress-strain behaviour is shown in Figure 4 a) and the corresponding strain response over time is shown in Figure 4 b). Rapid unloading, after an extended holding time, was found to cause issues with the control parameters of the load frame. This was avoided by adding a small loading/unloading step of ±10 MPa, after the end of the holding time. It can be seen from Figure 4 that increasing the loading rate resulted in an almost linear strain response for both materials, followed by a time-dependent strain response during the holding time at –500 MPa. Rapid loading allows for the determination of the elastic and plastic contributions. Linear fits of these regions have slopes of 82 and 99 GPa, for the BSCF and the BSCF-BC material, respectively. During unloading there was again a nearly linear strain response and a subsequent decay in the remanent strain during the holding time at preload. Overall, the remanent strain increased to –0.15% and –0.10% for BSCF and BSCF-BC, respectively, which is nearly 3 to 4 times larger than during loading/unloading at 5 MPa/s. This is due to the faster loading rate reducing the remanent strain decay during unloading.

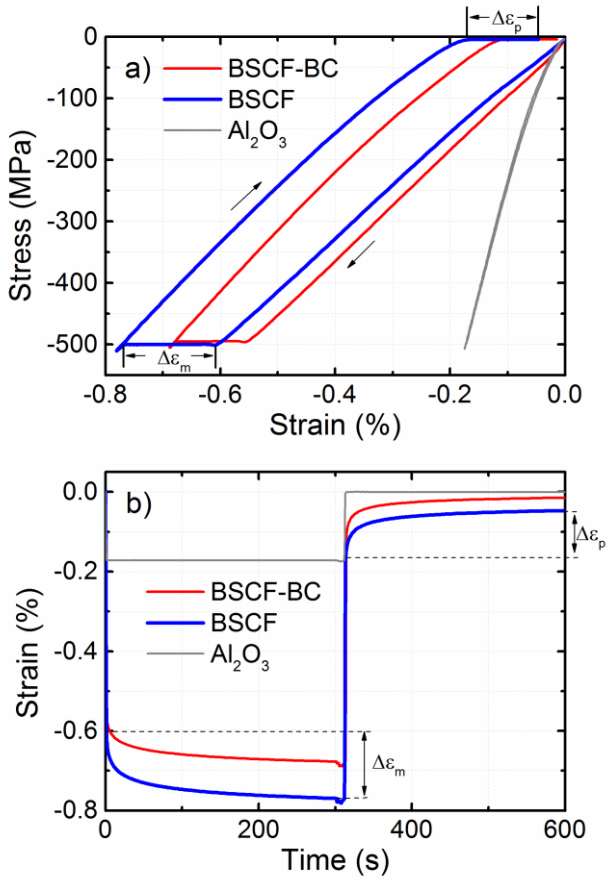

Figure 4. a) Stress-strain behaviour of BSCF and BSCF-BC annealed in air with loading rates of –500 MPa/s and holding times of 5 min and b) corresponding strain over time. $\Delta\varepsilon_m$ and $\Delta\varepsilon_p$ indicates relaxation strain at maximum (–500 MPa) and pre-load (–3.8 MPa) state, respectively. Al_2O_3, a linear material is shown for comparison and does not exhibit such strain relaxation.

During the holding time at maximum stress and preload, the samples were found to display a creep-type behaviour, shown in Figure 4 b). The relaxation strains $\Delta\varepsilon_m$ at maximum load are –0.16% and –0.12% for BSCF and BSCF-BC, respectively. In contrast, the relaxation strains at preload $\Delta\varepsilon_p$ are 0.13% and 0.10% for BSCF and BSCF-BC, respectively. It is apparent that nearly 80% of the remanent strain is lost during the relaxation process at preload, indicating that the creep-type process responsible for the nonlinear mechanical behaviour is also reversible upon unloading.

Phenomenologically, this behaviour is similar to room temperature creep in PZT, which is based on ferroelastic domain wall motion. The interaction of domain wall motions with defect dipoles, *e.g.,* oxygen vacancies, play a significant role in the stress-strain behaviour. The vacancies are able to diffuse over time, enabling delayed domain wall motion and resulting in a time dependent deformation [51].

3.3 Stress Dependent In Situ Synchrotron XRD

In situ high energy X-ray diffraction experiments can provide useful information regarding the structural origin of field-induced behaviour in advanced functional materials as some mechanisms may be transient [52]. A uniaxial compressive stress was applied on an air annealed BSCF-BC sample, while continuously measuring the diffraction pattern in transmission geometry. Cascade plots of the (100), (110), and (111) reflections at selected stress levels during loading and unloading from the maximum applied stress of –720 MPa are shown parallel and perpendicular to the loading axis in Figure 5 a) and b), respectively. A significant change of intensities or evolution of new reflections could not be observed in the stress-dependent diffraction patterns, strongly indicating that the origin of the nonlinear mechanical behaviour is not related to the stress-induced change of crystallographic symmetry or domain switching.

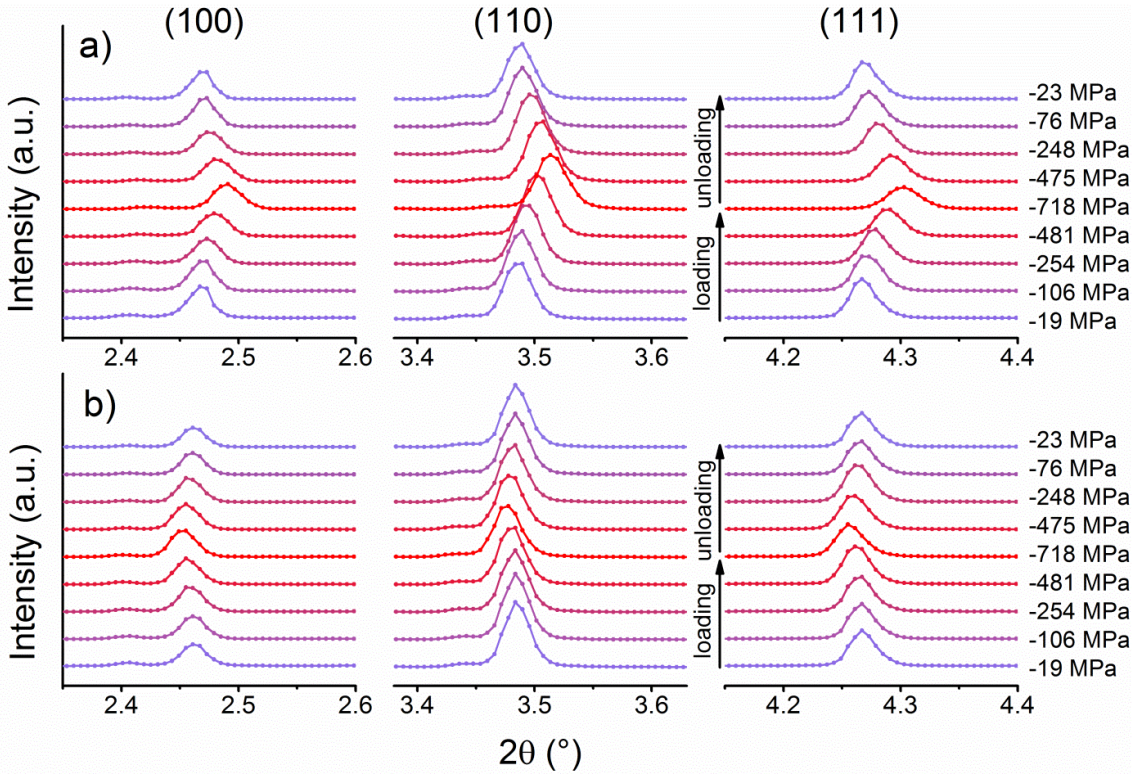

Figure 5. Cascade plots of the (100), (110) and (111) reflections (a) parallel and (b) perpendicular to the loading axis for a selection of different stress steps between preload and –720 MPa.

As compressive load is increased, the reflections parallel to the load axis are shifted to higher 2θ angles, i.e., lattice plane distances, d_{hkl}, decrease along the compressive loading axis (Fig. 5 a). Perpendicular to the loading axis, the reflections are shifted to smaller 2θ angles because of lateral expansion perpendicular to the loading direction. Upon unloading, the reflections shift back to the initial position, which is consistent with elastic behaviour of crystalline materials. Using the peak positions, the lattice strain $\varepsilon_{lattice}$ can be calculated from the *in situ* diffraction data using the Eq. (1):

$$\varepsilon_{lattice}(\sigma) = \frac{d_{hkl}(\sigma) - d_{hkl}(0)}{d_{hkl}(0)} \quad (1)$$

where $d_{hkl}(0)$ and $d_{hkl}(\sigma)$ are the lattice plane distances for the stress-free and stress-dependent state. Calculated lattice strains are shown in Figure 6 a) – c).

Figure 6 d) compares the macroscopic stress-strain curve of BSCF-BC annealed in air to the stress-lattice-strain curve determined from the evolution of the (100) reflection. The macroscopic measurement was performed under similar conditions, namely a 0.5 MPa/s loading/unloading rate and a maximum stress of –720 MPa.

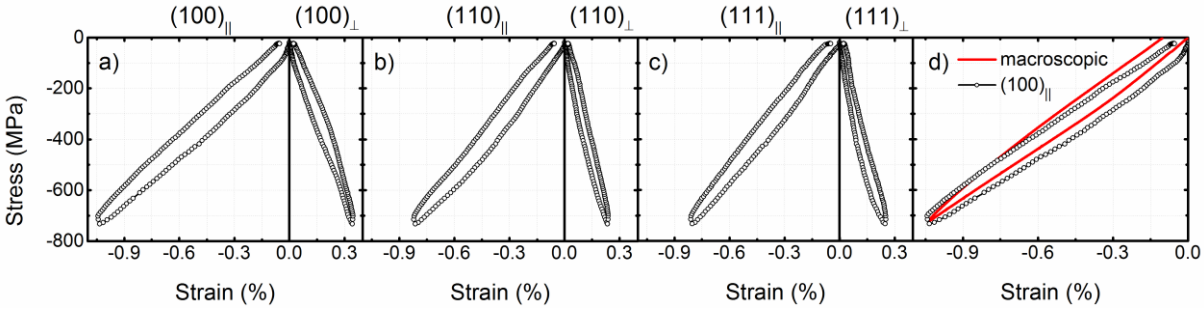

Figure 6. Stress-lattice-strain curves calculated from stress induced shifts of (100), (110) and (111) reflections parallel and perpendicular to the loading axis. A macroscopic stress-strain curve with similar loading parameters is included for comparison.

The stress–lattice-strain and macroscopic stress-strain curves are in good agreement. Although the nonlinear mechanical behaviour is visible in the lattice strain as well, there is no direct clarification of the mechanism responsible for the nonlinearity. From the stress-lattice-strain behaviour it is possible to determine the Poisson's ratio along the <100>, <110>, and <111> crystallographic orientation using Eq. (2):

$$\nu = -\frac{\varepsilon_{\perp}}{\varepsilon_{\parallel}} \tag{3}$$

where $\varepsilon_{\perp}$ and $\varepsilon_{\parallel}$ are the strain values in the perpendicular (azimuth 90°) and axial (azimuth 0°) loading directions, respectively. Interestingly, the Poisson's ratio of the (100) reflection was found to be 0.37, significantly larger than for the (110) and (111) reflections, which were determined to be 0.29 and 0.26, respectively. The secant moduli are 71 GPa, 90 GPa and 91 GPa for the three crystallographic directions

<100>, <110> and <111>, respectively. Variations in the elastic properties of lattice indicate elastic anisotropy, despite the cubic crystal symmetry.

3.4 Oxygen Non-Stoichiometry

Through annealing BSCF samples in atmospheres with varying oxygen partial pressures it is possible to adjust different oxygen non-stoichiometry. In the present study, annealing in air and nitrogen resulted in oxygen non-stoichiometries of δ_{air} = 0.63(2) and δ_{N2} = 0.70(2), as revealed by powder neutron diffraction. To determine whether the oxygen vacancy concentration can influence the mechanical behaviour, a sample annealed in air and a sample annealed in nitrogen were applied with a step functional loading program, described previously in Sec. 3.1. The resulting stress-strain behaviour is shown in Figure 7.

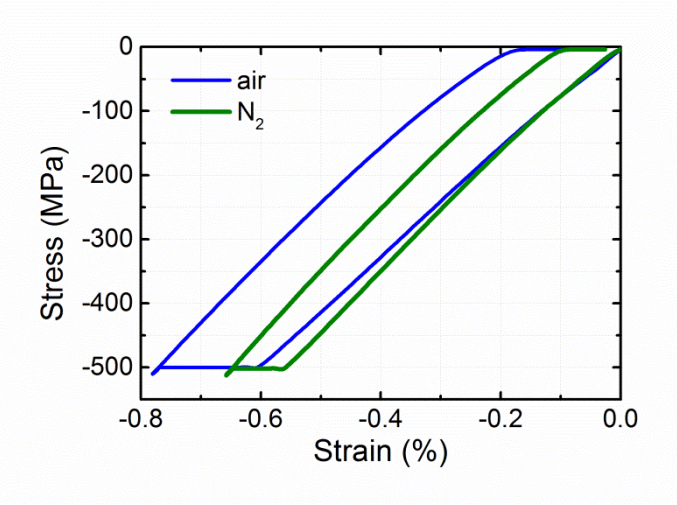

Figure 7. Stress-strain curves obtained for BSCF samples annealed at 900 °C for 2 hr in either an air and nitrogen atmosphere.

Both samples display the same nonlinear behaviour, namely an approximately linear stress-strain during loading and unloading as well as by the development of a

relaxational strain during the holding time at maximum stress and preload. Interestingly, however, the annealing atmosphere was found to reduce the relaxation strains of the nitrogen annealed samples by approximately 50%. Relaxation strains of $\Delta\varepsilon_{m,air}$ = -0.163% and $\Delta\varepsilon_{p,air}$ = 0.123% were observed for air annealed samples, in contrast to relaxation strains of $\Delta\varepsilon_{m,\ BSCF(N2)}$ = -0.085% and $\Delta\varepsilon_{p,\ BSCF(N2)}$ = 0.067% for nitrogen annealing. In addition, there is an apparent increase in the elastic modulus from 82 GPa in the air annealed samples to 89 GPa in the nitrogen annealed sample as measured by the slope of the stress-strain curve. Araki *et. al.* [36] and Huang *et. al.* [37] have reported smaller values for the elastic modulus at room temperature between 60 GPa and 65 GPa, by compressive experiments and ring-on-ring tests. Malzbender *et. al.* [53] found stiffness values between 60 GPa and 90 GPa by indentation, which are in fairly good agreement with the parameters obtained in this work. The strong influence of annealing atmosphere on the mechanical behaviour suggests that the mechanism of the nonlinearity is linked to oxygen vacancies, as it cannot be explained by ferroelasticity or field-induced phase transformations.

We propose a nonlinear strain mechanism based on the stress-induced local reorientation, i.e. migration of oxygen vacancies. As a simple matter of fact, a compression or expansion of the cubic unit cell along the <001> crystallographic direction must result in a local decrease of the symmetry to tetragonal. Using group-subgroup relationships [54], one can see that the highest symmetric tetragonal subgroup of $Pm\bar{3}m$ is $P4/mmm$, and even for this symmetry, a splitting of the anion site (3*c* for $Pm\bar{3}m$) into two crystallographic independent sites (1*c* and 2*e* for $P4/mmm$) would be found. This results in an energetically non-equivalence of the 1*c* and 2*e* sites, which might have an impact on the distribution of vacancies within BSCF once a mechanical load has been applied.

The A-site and B-site cations around an oxygen vacancy repel each other, as their positive charge cannot be compensated by the negative charge of the oxygen anion in between. The coulomb repulsion between two B-site cations can be expected to be stronger than the repulsion between two A-site cations, as the B-site cations have higher charge (+II, +III) and are chemically harder than A-site cations. This can lead to a distortion of the cubic unit cell or an overall lowering of symmetry if the vacancies can order within a 3-dimensional pattern (see [55,56], where for BSCF the cubic symmetry is maintained).

The extraordinary high vacancy concentration of δ ≈ 0.6 to 0.7 implies, on average, more than one out of every six oxygen sites in the oxygen octahedron, coordinating the B-site cation, is vacant. In the initial state, the oxygen vacancies are more or less randomly distributed throughout the lattice. However, for a loaded state, alignment of vacancies in a certain manner due to an increased distortion of the unit cell and, therefore, lowering of symmetry, could result in an anisotropic strain, which could then be affected by the external mechanical field.

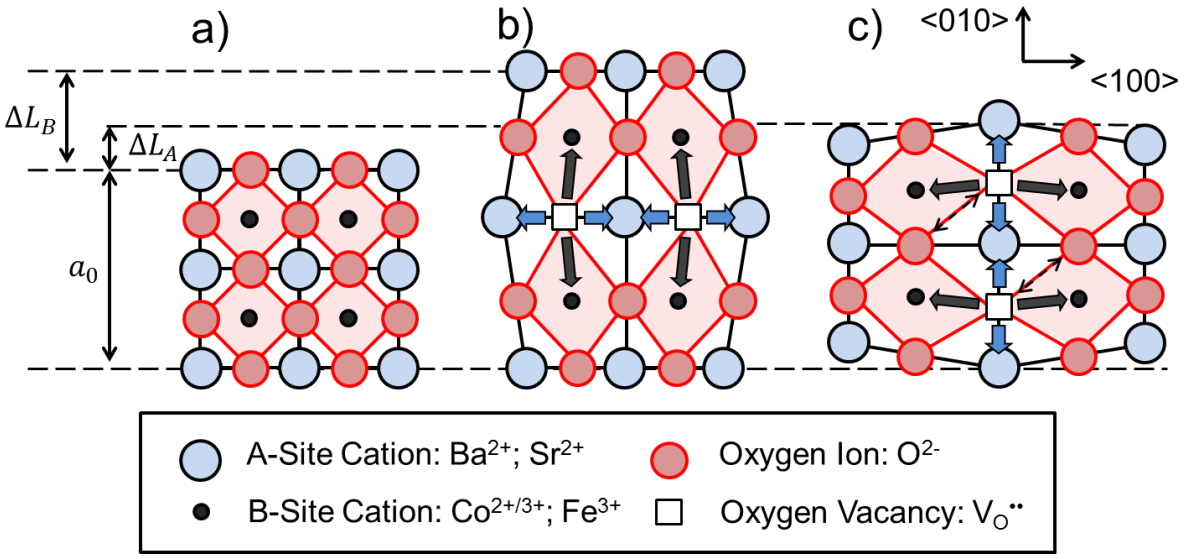

Figure 8. a) Schematic of a projection along the <001> crystallographic direction of a 2x2 ideal cubic BSCF super cell without any defects, which has the lattice parameter a_0. b) A set of oxygen vacancies in horizontal alignment leads to cation repulsion,

which is stronger in vertical direction, i.e., B-site cations. c) Migration of the oxygen vacancies to vertical alignment leads to stronger repulsion in horizontal direction and weaker repulsion in vertical direction. The distortion is exaggerated in order to explain the mechanism.

We suggest the following scenario: If a BSCF crystallite, with oxygen vacancies aligned as shown in Figure 8 b), is vertically compressed, the B-Site cations (which are unshielded by oxygen ions) would be forced closer together. As the charge in between them is not compensated by an oxygen ion, this alignment must be expected to be energetically unfavourable. An oxygen ion from a neighbouring site could migrate between the two B-site cations, which are pressed together, in order to shield their charge from each other. Therefore, the B-site cations could vertically relax closer together, leaving the structure as depicted in Figure 8 c). The vertical displacement gained by local vacancy migration is the difference between die displacements caused by A-site and B-Site cation repulsion $\Delta L_B - \Delta L_A$.

As observed in the stress-strain curves, annealing BSCF in nitrogen resulted in a decrease of relaxation strain, despite the nearly 10 % increase in oxygen vacancy concentration. Importantly, however, annealing of BSCF in nitrogen reduces some Co^{3+} ions to Co^{2+}, which also results in an increased average B-site cation radius (see Table 1). This means that the increased concentration of oxygen vacancies corresponds to a cationic radii increase as well, constricting the oxygen migration paths that possibly results in less local migration and, therefore, less strain. In addition, any oxygen non-stoichiometry value above $\delta = 0.5$ also means at least some of the B-site cations show 4-fold coordination. Statistically, this can result in reduced oxygen migration as the preferred migration path of an oxygen vacancy might already be occupied by another vacancy. Furthermore it has to be noted that

increasing oxygen vacancy concentration leads to decreasing mobility due to enhanced formation defect associates [57].

In general the strain mechanism observed in BSCF could also be based on a spin-state transition of the B-site cobalt ion, as suggested by Araki *et al.* [36,40]. Cobalt can exist in +II and +III oxidation state, with the latter possessing stability in either high spin or low spin state, depending on temperature and structural arrangement. Iron has a higher electronegativity and is known to be mainly +III in BSCF [58]. The magnitude of the magnetic moment is given by Eq. (4):

$$\left|\vec{M}\right| = 2 \cdot \sqrt{S \cdot (S+1)} \tag{4}$$

The refined magnetic moments of 2.33(2) μ_B and 2.61(2) μ_B of the B-site cations in BSCF(air) and BSCF(N_2), respectively are rather small. This indicates that Co^{3+} is mainly present in the low-spin configuration while in a stress free state.

The Co^{3+} ion is a weakly Jahn-Teller active cation (see table 1), and therefore local symmetry lowering might also interfere with the spin state. This distortion would be expected to be lower for the Co^{2+} high-spin ion. A uniaxial compressive stress field may therefore induce a spin-state transition of the Co^{3+} ion, as a tetragonal distortion, i.e., the symmetry of a compressed/elongated octahedron increases the stability of the high-spin state. After reducing BSCF by thermal treatment in nitrogen, the oxygen vacancy concentration increases from 0.63(2) to 0.70(2), corresponding to a decrease in the ratio of (Co^{3+}/Co^{2+}) from (67.5% / 32.5%) to (50% / 50%). A lower amount of Jahn-Teller active species might result in less distortion. This may be an alternative explanation for the nonlinear strain mechanism in BSCF.

Table 1. Ionic properties of cobalt

Ion	Co^{2+} low-spin*	Co^{2+} high-spin	Co^{3+} low-spin	Co^{3+} high-spin
Total spin S	0.5	1.5	0	2
Jahn-Teller-Effect	strong	very weak	none	weak
Proportion (air)	32.5%		67.5%	
Proportion (N_2)	50%		50%	

**Co^{2+} low-spin is unlikely to be stable in oxides [59]*

It is important to note that both mechanisms described here cannot be validated or falsified with the experimental techniques used in this work. Additional measurements, such as stress-dependent *in situ* neutron diffraction or stress-dependent SQUID measurements, might give more insight into the nature of the nonlinear deformation of BSCF, particularly the effect of stress on the spin transition. In addition, stress-dependent electron paramagnetic resonance might also be able to show the local reorientation of oxygen vacancies, however such measurements would be challenging due to the polycrystalline nature of the sample.

4. Conclusions

The mechanical behaviour of polycrystalline BSCF was analysed by triangular and step functional compressive testing. The strain response consists of a linear elastic and a nonlinear time-dependent plastic contribution. It was shown through annealing experiments that the magnitude of the nonlinear contribution decreased with increasing oxygen vacancy concentration. *In situ* stress-dependent synchrotron XRD measurements reveal that the nonlinearity is also present at the microscopic length scales. The origin of this phenomenon cannot be attributed to the ferroelasticity or a phase transformation. These results suggest that the mechanism of the nonlinear

mechanical behaviour may be based on local oxygen vacancy migration or a spin-state transition.

Acknowledgements

This project was funded by the Deutsche Forschungsgemeinschaft under WE 4972/2-1 and benefited from the support of CL551/2-1 and HI 1867/1-1.

References

[1] D. Chen, Z. Shao, International Journal of Hydrogen Energy 36 (2011) 6948–6956.
[2] J.F. Vente, S. McIntosh, W.G. Haije, H.J.M. Bouwmeester, J Solid State Electrochem 10 (2006) 581–588.
[3] Z. Shao, S.M. Haile, Nature 431 (2004) 170–173.
[4] H. Wang, Y. Cong, W. Yang, Journal of Membrane Science 210 (2002) 259–271.
[5] S.B. Adler, Chem. Rev. 104 (2004) 4791–4844.
[6] H. Ullmann, N. Trofimenko, F. Tietz, D. Stöver, A. Ahmad-Khanlou, Solid State Ionics 138 (2000) 79–90.
[7] S. McIntosh, J.F. Vente, W.G. Haije, D.H.A. Blank, H.J.M. Bouwmeester, Chem. Mater. 18 (2006) 2187–2193.
[8] A.A. Yaremchenko, S.M. Mikhalev, E.S. Kravchenko, J.R. Frade, Journal of the European Ceramic Society 34 (2014) 703–715.
[9] B. Rutkowski, R. Kriegel, J. Malzbender, Journal of Membrane Science 462 (2014) 69–74.
[10] W. Araki, Y. Imai, T. Adachi, Journal of the European Ceramic Society 29 (2009) 2275–2279.
[11] W. Araki, M. Kuribara, Y. Arai, Solid State Ionics 193 (2011) 5–10.
[12] E. Bucher, A. Egger, P. Ried, W. Sitte, P. Holtappels, Solid State Ionics 179 (2008) 1032–1035.
[13] Y. Hayamizu, M. Kato, H. Takamura, Journal of Membrane Science 462 (2014) 147–152.
[14] R. Kriegel, R. Kircheisen, J. Töpfer, Solid State Ionics 181 (2010) 64–70.
[15] P. Zeng, Z. Chen, W. Zhou, H. Gu, Z. Shao, S. Liu, Journal of Membrane Science 291 (2007) 148–156.
[16] A.V. Virkar, R.L.K. Matsumoto, J American Ceramic Society 69 (1986) C-224-C-226.
[17] M.I. Morozov, M.-A. Einarsrud, J.R. Tolchard, P.T. Geiger, K.G. Webber, D. Damjanovic, T. Grande, J. Appl. Phys. 118 (2015) 164104.

[18] S.C. Hwang, C.S. Lynch, R.M. McMeeking, Acta Metallurgica et Materialia 43 (1995) 2073–2084.
[19] E.A. McLaughlin, T. Liu, C.S. Lynch, Acta Materialia 53 (2005) 4001–4008.
[20] M. Davis, D. Damjanovic, N. Setter, Phys. Rev. B 73 (2006).
[21] M. Budimir, D. Damjanovic, N. Setter, Phys. Rev. B 72 (2005).
[22] X. Tan, E. Aulbach, W. Jo, T. Granzow, J. Kling, M. Marsilius, H.-J. Kleebe, J. Rödel, J. Appl. Phys. 106 (2009) 44107.
[23] F.H. Schader, Z. Wang, M. Hinterstein, J.E. Daniels, K.G. Webber, Phys. Rev. B 93 (2016).
[24] J.E. Daniels, G. Picht, S. Kimber, K.G. Webber, Appl. Phys. Lett. 103 (2013) 122902.
[25] T. Leist, K.G. Webber, W. Jo, E. Aulbach, J. Rödel, A.D. Prewitt, J.L. Jones, J. Schmidlin, C.R. Hubbard, Acta Materialia 58 (2010) 5962–5971.
[26] K.G. Webber, Y. Zhang, W. Jo, J.E. Daniels, J. Rödel, J. Appl. Phys. 108 (2010) 14101.
[27] C. Niedrig, S. Taufall, M. Burriel, W. Menesklou, S.F. Wagner, S. Baumann, E. Ivers-Tiffée, Solid State Ionics 197 (2011) 25–31.
[28] H. KRUIDHOF, H. BOUWMEESTER, R. VDOORN, A. BURGGRAAF, Solid State Ionics 63-65 (1993) 816–822.
[29] B. Rutkowski, J. Malzbender, T. Beck, R.W. Steinbrech, L. Singheiser, Journal of the European Ceramic Society 31 (2011) 493–499.
[30] B. Rutkowski, J. Malzbender, R.W. Steinbrech, T. Beck, H. Bouwmeester, Journal of Membrane Science 381 (2011) 221–225.
[31] J.X. Yi, H.L. Lein, T. Grande, S. Yakovlev, H. Bouwmeester, Solid State Ionics 180 (2009) 1564–1568.
[32] M.G. Sahini, J.R. Tolchard, K. Wiik, T. Grande, Dalton transactions (Cambridge, England 2003) 44 (2015) 10875–10881.
[33] J. Ovenstone, J.-I. Jung, J.S. White, D.D. Edwards, S.T. Misture, Journal of Solid State Chemistry 181 (2008) 576–586.
[34] M.M. Kuklja, E.A. Kotomin, R. Merkle, Y.A. Mastrikov, J. Maier, Physical chemistry chemical physics PCCP 15 (2013) 5443–5471.
[35] M.M. Kuklja, Y. Mastrikov, B. Jansang, E.A. Kotomin, Solid State Ionics 230 (2013) 21–26.
[36] W. Araki, J. Malzbender, Scripta Materialia 69 (2013) 278–281.
[37] B.X. Huang, J. Malzbender, R.W. Steinbrech, P. Grychtol, C.M. Schneider, L. Singheiser, Appl. Phys. Lett. 95 (2009) 51901.
[38] B.X. Huang, J. Malzbender, R.W. Steinbrech, L. Singheiser, Journal of Membrane Science 359 (2010) 80–85.
[39] B. Huang, J. Malzbender, R.W. Steinbrech, J. Mater. Res. 26 (2011) 1388–1391.
[40] W. Araki, Y. Arai, J. Malzbender, Materials Letters 132 (2014) 295–297.
[41] S. Svarcova, K. Wiik, J. Tolchard, H. Bopuwmeester, T. Grande, Solid State Ionics 178 (2008) 1787–1791.
[42] A.J. Studer, M.E. Hagen, T.J. Noakes, Physica B: Condensed Matter 385-386 (2006) 1013–1015.
[43] Bruker AXS, Topas V5, General profile and structure analysis software for powder diffraction data, User's Manual, Karlsruhe, Germany, 2014.

[44] O. Clemens, F.J. Berry, A.J. Wright, K.S. Knight, J.M. Perez-Mato, J.M. Igartua, P.R. Slater, Journal of Solid State Chemistry 206 (2013) 158–169.
[45] K.G. Webber, E. Aulbach, T. Key, M. Marsilius, T. Granzow, J. Rödel, Acta Materialia 57 (2009) 4614–4623.
[46] J.E. Daniels, M. Drakopoulos, Journal of synchrotron radiation 16 (2009) 463–468.
[47] A.P. Hammersley, S.O. Svensson, M. Hanfland, A.N. Fitch, D. Hausermann, High Pressure Research 14 (1996) 235–248.
[48] Bruker AXS, TOPAS V3.0: General profile and structural analysis software for powder diffraction data. User's Manual, Karlsruhe, Germany, 2005.
[49] R.W. Cheary, A.A.Coelho, J.P.Cline, Journal of Research of the National Institute of Standards and Technology (2004) 1–25.
[50] J. Sun, M. Yang, G. Li, T. Yang, F. Liao, Y. Wang, M. Xiong, J. Lin, Inorganic chemistry 45 (2006) 9151–9153.
[51] D. Zhou, M. Kamlah, Acta Materialia 54 (2006) 1389–1396.
[52] J.L. Jones, J Electroceram 19 (2007) 69–81.
[53] J. Malzbender, B. Huang, J. Mönch, R.W. Steinbrech, J Mater Sci 45 (2010) 1227–1230.
[54] H. Baerenighausen, Group-Subgroup Relations Between Space groups: A Usefull Tool in Crystal Chemistry, Karlsruhe, Germany, 1980.
[55] O. Clemens, Journal of Solid State Chemistry 225 (2015) 261–270.
[56] M.T. Anderson, J.T. Vaughey, K.R. Poeppelmeier, Chem. Mater. 5 (1993) 151–165.
[57] J. Kilner, Solid State Ionics 129 (2000) 13–23.
[58] M. Arnold, Q. Xu, F.D. Tichelaar, A. Feldhoff, Chem. Mater. 21 (2009) 635–640.
[59] B. Raveau, M. Seikh, Cobalt Oxides: From Crystal Chemistry to Physics, 1st ed., Wiley-VCH, s.l., 2012.